Northumbria Research Link

Northumbria
University
NEWCASTLE

Article

Highly efficient mixed-metal spinel cobaltite electrocatalysts for the oxygen evolution reaction

Leiming Tao [a,b], Penghu Guo [a], Weiling Zhu [a], Tianle Li [a], Xiantai Zhou [d], Yongqing Fu [c], Changlin Yu [a, #], Hongbing Ji [a,d, *]

[a] *School of Science, Guangdong University of Petrochemical Technology, Maoming 525000, Guangdong, China*
[b] *Wuhan National Laboratory for Optoelectronics, Huazhong University of Science and Technology, Wuhan 430074, Hubei, China*
[c] *Faculty of Engineering and Environment, Northumbria University, Newcastle upon Tyne, NE1 8ST, UK*
[d] *Fine Chemical Industry Research Institute, School of Chemistry, Sun Yat-sen University, Guangzhou 510275, Guangdong, China*

ARTICLE INFO

Article history:
Received 11 December 2020
Accepted 24 December 2020
Published 5 xxxxxx 2020

Keywords:
Cation-substituted spinel cobaltites
Crystal field
Oxygen evolution reaction
Water-splitting
Electrocatalysis

ABSTRACT

Cation substitution in spinel cobaltites (e.g., ACo_2O_4, in which A = Mn, Fe, Co, Ni, Cu, or Zn) is a promising strategy to precisely modulate their electronic structure/properties and thus improve the corresponding electrochemical performance for water splitting. However, the fundamental principles and mechanisms are not fully understood. This research aims to systematically investigate the effects of cation substitution in spinel cobaltites derived from mixed-metal-organic frameworks on the oxygen evolution reaction (OER). Among the obtained ACo_2O_4 catalysts, $FeCo_2O_4$ showed excellent OER performance with a current density of 10 $mA \cdot cm^{-2}$ at an overpotential of 164 mV in alkaline media. Both theoretical calculations and experimental results demonstrate that the Fe substitution in the crystal lattice of ACo_2O_4 can significantly accelerate charge transfer, thereby achieving enhanced electrochemical properties. The crystal field of spinel ACo_2O_4, which determines the valence states of cations A, is identified as the key factor to dictate the OER performance of these spinel cobaltites.

1. Introduction

Solar or wind energy can be converted from electricity into chemical energy, and hydrogen fuel can be generated and stored by means of water splitting. During water splitting, the reaction kinetics of the oxygen evolution reaction (OER) at the anode are typically much slower than those of the hydrogen evolution reaction at the cathode. [1]. Therefore, it is critical to accelerate the rate of the OER at the anode and improve the overall efficiency of water-splitting. Currently, iridium dioxide

* Corresponding author. Tel/Fax: +86-0668-2923081; E-mail: jihb@mail.sysu.edu.cn
# Corresponding author. E-mail: yuchanglinjx@163.com
This study was supported by the National Natural Science Foundation of China (21938001, 21576302, 21878344, 21961160741), Natural Science Foundation of China- SINOPEC Joint fund (U1663220), Featured Innovation Project of Guangdong Education Department (2018KTSCX144, 2016KTSCX087), Guangdong Provincial Key R&D Programme (2019B110206002), the Local Innovative and Research Teams Project of Guangdong Pearl River Talents Program (2017BT01C102), Scientific Research Fund of Natural Science Foundation of Guangdong University of Petrochemical Technology (2019rc019, 2019rc053), Guangdong Province Universities and Colleges Pearl River Scholar Funded Scheme (2019), Key Natural Science Reserch Projects of Guangdong Provincial Universities (2019KZDXM010)，and Guangdong Basic and Applied Basic Research Foundation (2019A1515011249). This work was financially supported by the UK Engineering and Physical Sciences Research Council (EPSRC) for support under grant EP/P018998/1, and Newton Mobility Grant (IE161019) through the Royal Society and the National Natural Science Foundation of China.
DOI: 10.1016/S1872-2067(20)63638-5 | http://www.sciencedirect.com/science/journal/18722067 | Chin. J. Catal., Vol. 41, No. 0, xxxxxx 2020

(IrO_2) and ruthenium dioxide (RuO_2) have been commonly used as OER catalysts. However, the most frequently used electrocatalysts, IrO_2 and RuO_2, are not only expensive but also have unsustainable supply and environmental issues. Hence, it is critical to develop non-noble and abundant metal-based electrocatalysts for the OER, with good catalytic activity and high durability for practical applications in water splitting. To date, huge efforts have been made to develop transition metal oxides/hydroxides [2], phosphate [3], and sulfides [4] for the OER.

Three-dimensional metal-based spinel oxides have recently attracted enormous attention due to the wide range of technological applications in the semiconductor industry, such as high-frequency devices, catalysts, magnetic recordings, biomedical devices, microwave absorbers, gas sensors, and optical materials/devices [5–8]. They possess a stoichiometric AB_2O_4 cubic structure, where A and B stand for tetrahedral and octahedral configurations of transition metals, respectively [9]. Because of highly distributed metal cations A and B between each position with different oxidation states in the spinel structure AB_2O_4, the mixed-transition metal spinel structures exhibit various interesting physical and chemical properties, particularly in the catalytic field. The partially filled nature of the 3*d* transition metal orbitals enables the electron transfer process, which plays a key role in creating excellent magnetic, electronic, and electrochemical properties. These provide us with an opportunity to tune their electrical structures at the atomic scale to achieve highly efficient water splitting electrocatalysts and further match the demand for electrolyzers and fuel cells, etc. [10]. Recently, there has been an increased interest in using mixed-metal spinel oxides for the OER applications [11–14].

However, the relationship between the electrocatalytic performance of the mixed-metal spinel oxides and their elementary compositions, valence states, and distribution of sites is still not fully understood. Experimental observations and theoretical analyses have been performed [15–18] to identify the exact roles of spinel oxides in the OER. For example, Prabu et al. [19] found that Ni^{3+} ion substitution at the octahedral sites of the $NiCo_2O_4$ can significantly enhance the OER performance. Hutchings et al. [20] reported that the active sites of Co_3O_4 for the OER are mainly the octahedral sites of Co^{3+}. Wei et al. [17] identified that Mn^{3+} ions in the octahedral positions of $MnCo_2O_4$ are the active sites for the OER. These well-documented studies clearly indicate that electrocatalytic performances of the cobalt-based spinel oxides for the OER strongly depend on the valence states of transition metal cations (A) and their corresponding site distributions in the ACo_2O_4 spinel structure [10]. The substitution of transition metal cations (A) can be a promising strategy for precisely modulating the electronic properties and optimizing the electrochemical OER performance of cobalt-based spinel oxides (e.g., ACo_2O_4, in which A = Mn, Fe, Co, Ni, Cu, or Zn).

In this paper, we report a series of the cobalt-based spinel oxides with well-defined compositions and morphologies, derived from the precursor mixed-metal-organic frameworks (MMOFs). A site substitution by different transition metal cations in cobalt-based spinel oxides and their corresponding OER behavior have been discussed in detail. Among these ACo_2O_4, $FeCo_2O_4$ showed an excellent catalytic activity with a current density of 10 $mA \cdot cm^{-2}$ at an overpotential of 164 mV in alkaline media. Furthermore, charge transport, electronic structure, and spinel crystal fields of these ACo_2O_4 were systematically investigated based on experimental studies and density functional theory (DFT) calculations. The underlying mechanisms for the enhanced electrocatalytic performance induced by substitutions of cations with different numbers of d-electrons between 5 and 10 have also been clarified.

2. Experimental

2.1. Synthesis of $FeCo_2$-PTCDA MMOFs.

In a typical synthesis process [21], $Fe(OAc)_2 \cdot 2H_2O$ (0.133 mmol) and $Co(OAc)_3 \cdot 4H_2O$ (0.267 mmol) were dissolved in 22.5 mL deionized water, and PTCDA (0.2 mmol) was dissolved in 12.5 mL NaOH solution (0.8 mmol NaOH). The PTCDA solution was added dropwise to the mixed solution of metal acetates under constant stirring. The immediate formation of a precipitate was observed. The reaction mixture was stirred at room temperature for 30 min, and then transferred into a Teflon-lined stainless steel vessel (45 mL) and heated at 100 °C for 8 h. After cooling down to room temperature, the precipitate was collected by centrifugation, washed with water and dried.

The obtained $FeCo_2$-PTCDA MOFs were annealed at 400 °C in the air for 1 h with a heating ramp of 1 $°C \cdot min^{-1}$. For the synthesis of other ACo_2-PTCDA (A = Zn, Cu, Ni, Co, and Mn) MMOFs, the processes are similar to those described above for the $FeCo_2$-PTCDA, except for the choice of metal acetates.

2.2. Catalyst characterization

Morphologies, chemical compositions, and crystalline structures of all the samples were characterized using various methods. The X-ray diffraction (XRD) measurements were performed using an X'pert PRO diffractometer (PANalytical B.V.) with a Cu K_α X-ray source operated at 40 kV and 40 mA. Surface and internal microstructures were investigated using field emission scanning electron microscopy (FE-SEM, Nova NanoSEM 450) and high-resolution transmission electron microscopy (HR-TEM, 300 kV Titan Probe corrected TEM, Titan G2 60-300). Surface chemical states of the samples were analyzed using an X-ray photoelectron spectroscopy (XPS, Thermofisher-ESCALab 250). The shift of the core-level spectra was calibrated using the C 1*s* neutral carbon peak at 284.8 eV. The Brunauer-Emmett-Teller (BET) surface area (S_{BET}) and pore size distribution were determined using a Micromeritics ASAP 2000 nitrogen adsorption apparatus. All the samples were degassed at 180 °C prior to the BET measurements.

2.3. Electrochemical measurements

The catalytic activity of the prepared ACo_2O_4 loaded onto standard glassy carbon electrodes was evaluated using elec-

trochemical measurements for the OER with a three-electrode electrochemical cell in 1 M KOH aqueous solution as the electrolyte. To prepare the electrode, 2 mg ACo_2O_4 sample was dispersed into a 1 mL mixture of water, ethanol, and Nafion solution (5 wt% in a mixture of lower aliphatic alcohols and water, Aldrich) with a volume ratio of 1:3.85:0.15, under a constant ultra-sonication for 10 min. The final catalyst ink suspension had a concentration 2.0 mg·mL^{-1}, and its suspension of 19.8 μL was then transferred onto a polished glassy-carbon electrode of 5 mm in diameter, resulting in a mass loading of 0.2 mg·cm^{-2}.

Cyclic voltammetry (CV) and linear sweep voltammetry (LSV) were conducted using an electrochemical station (CHI 750D, CH Instruments). Standard glassy carbon (GC) electrode (5 mm in diameter, Pine Instruments) was used as the working electrode. Hg/HgO was used as the reference electrode, and a graphite electrode was used as the counter electrode. Tafel plots of the samples were obtained similar to those reported in the literature [22,23]. LSV curves and Tafel plots were recorded at two different scan rates of 5 and 0.1 mV·s^{-1}, respectively. Electrochemical impedance spectroscopy (EIS) was used (Autolab PGSTAT302N) with a frequency range from 0.01 Hz to 1 MHz and a potential amplitude of 10 mV. Impedance value (R) of the 1 M KOH solution was measured to be 6.9 Ω at room temperature. Unless stated otherwise, the tests were made without iR compensation in 1 M KOH solution.

Measurements using rotating ring-disk electrodes (RRDEs) were conducted in 1 M KOH electrolyte at room temperature using a three-electrode system (Pine Instruments and WaveDriver Workstation). The measurement was conducted in a solution of N_2-saturated 1 M KOH for seven times with various rotation speeds (i.e., 400, 620, 900, 1225, 1600, 2025, 2500 rpm). The Tafel slope was calculated using the Koutecký-Levich equation with the RRDE for the OER without *i*R [24]:

$$\frac{1}{i}=\frac{1}{i_K}+\frac{1}{i_L}=\frac{1}{i_K}+\frac{1}{0.62nFAD_0^{2/3}\omega^{1/2}\nu^{-1/6}C_0^*} \quad (1)$$

The electrochemical surface area (ECSA) of the catalyst plays a crucial role in electrochemical reactions. To study the ECSA of ACo_2O_4, we conducted cyclic voltammograms at different scan rates (10, 20, 30, 40, 50, 60, 70, 80, 90, 100, 110, and 120 mV·s^{-1}) in a non-faradaic potential region. The ECSA is the product of R_FS, in which R_F stands for the roughness factor, which is obtained from the ratio of C_{dl} of the test sample and the C_s (= 60 μF·cm^{-2}) of a smooth surface [25]. S stands for the real surface area of the smooth metal electrode, which generally equals the geometric area of the carbon electrode [26]. The values of C_{dl} were obtained using cyclic voltammetry, and the results are shown in Fig. S3. As shown in Fig. S3, the C_{dl} were obtained to be 8, 5.4, 5.3, 3.7, 2.6 and 1 mF·cm^2 for $ZnCo_2O_4$, Co_3O_4, $NiCo_2O_4$, $MnCo_2O_4$, $FeCo_2O_4$, and $CuCo_2O_4$, respectively.

The faradaic efficiency (FE) was obtained according to the method reported in the literature [27]. The FE (or current efficiency) is defined as the ratio of the measured amount of produced oxygen and the theoretical amount of produced oxygen, according to Faraday's Law. It can be calculated as follows:

$$\eta = 4(N \times F)/(I \times t) \quad (2)$$

where η is the theoretical yield (current efficiency); N stands for the Molar amount of produced oxygen; I represents the current in ampères; t is the time in seconds (in this work, t = 1 min); 4 is the oxidation state (number of displaceable electrons per O_2); and F is Faraday's constant, F = 96487 C·mol^{-1}.

Chronopotentiometry was applied at a given potential (1.53 V) to maintain constant O_2 generation. N_2 was constantly purged into the cathodic compartment at a flow rate of 5 cm^3·min^{-1}, and the compartment was connected to the gas-sampling loop of a gas chromatograph (GC2020, Hubei Hengxinshiji Scientific Instrument Co.). A thermal conductivity detector (TCD) was used to detect and quantify the generated O_2.

All the measured potentials were calibrated using a reversible hydrogen electrode (RHE) based on the following equation:

$$E_{RHE} = E_{Hg/HgO} + 0.098V + 0.059pH \quad (3)$$

2.4. Density functional theory calculations

All the DFT calculations were performed using the Vienna Ab initio Simulation Package (VASP) [28]. The interaction between core ions and valence electrons was described by the projector augmented wave (PAW) method [29], while the generalized gradient approximation (GGA) with the Perdew-Burke-Ernzerhof (PBE) function was used for electron exchange-correlation interactions [30]. The energy cut-off for the plane waves was chosen to be 520 eV. To correctly describe the electronic structure of the A-3d states (A = Mn, Fe, Co, Ni, Cu, and Zn), a rotational invariant type GGA+U method, as proposed by Dudarev et al. [31], was employed. The effective on-site Coulomb terms (U values) for the 3d states of Mn, Fe, Co, Ni, Cu, and Zn were selected to be 5.5, 3, 4.5, 10.5, 4.5, and 10 eV, respectively. The Monkhorst-Pack scheme sampling with a 2 × 2 × 2 k-point mesh was adopted for the integration in the irreducible Brillouin zone. The structural parameters of the ACo_2O_4 were obtained based on the XRD analysis. The lattice parameters and atomic positions were fully relaxed and calculated using the hybrid HSE06 functional, and the final forces on the relaxed atoms were less than 0.05 eV·A^{-1}. Spin-polarized calculations and ferromagnetic ordering were employed for all the cases.

3. Results and discussion

To identify the exact role of spinel oxides (Figs. S1 and S2), the ACo_2O_4 with well-defined morphologies and compositions was synthesized under a controlled temperature as low as 350 °C [21]. The OER activities of ACo_2O_4 samples were investigated using a standard three-electrode configuration with 1 M KOH aqueous solution at 25 °C. Figs. 1(a) and 1(b) show the OER specific activities of $ZnCo_2O_4$ (curve 1), $CuCo_2O_4$ (curve 2), $NiCo_2O_4$ (curve 3), Co_3O_4 (curve 4), $FeCo_2O_4$ (curve 5), and $MnCo_2O_4$ (curve 6) at a scan rate of 5 mV·s^{-1} after correction by removing the contribution of ECSA (Fig. S3). We compared the Tafel plots and overpotentials at 10 mA·cm^{-2} using various OER catalysts (Fig. 1(c)). The catalytic dynamics in terms of the turnover frequency (TOF) were further analyzed for ACo_2O_4

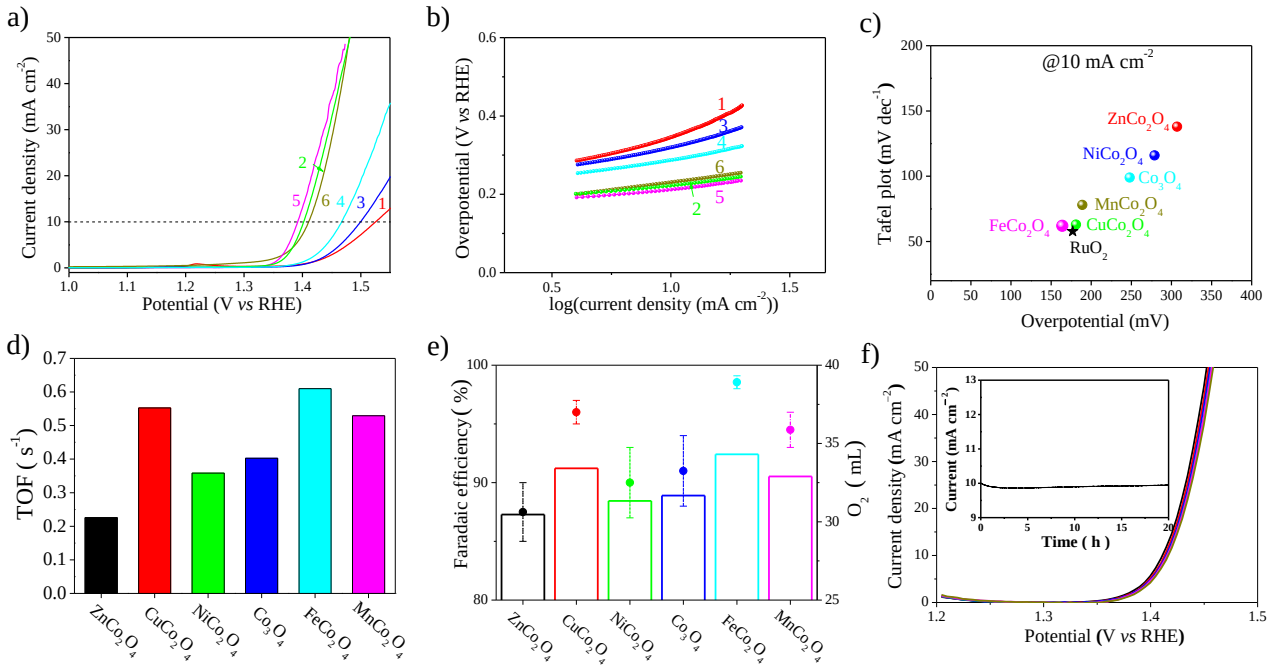

Fig. 1. Electrochemical measurements: (a) linear sweep polarization curves (LSV) of $ZnCo_2O_4$ (1), $CuCo_2O_4$ (2), $NiCo_2O_4$ (3), Co_3O_4 (4), $FeCo_2O_4$ (5), and $MnCo_2O_4$ (6) for the OER specific activities (corrected by removing the contribution of ECSA) in 1 M KOH; (b) Tafel slopes; (c) Tafel slope versus overpotential at 10 mA·cm^{-2} for reported OER catalysts; (d) Turnover frequency (TOF) of specific activity for ACo_2O_4; (e) FE for the OER, and the average oxygen production of ACo_2O_4; (f) Chronoamperometric response recorded using $FeCo_2O_4$, initially and after 10000 cycles with a scan rate of 100 mV·s^{-1}, at a constant overpotential to reach a current density of 10 mA·cm^{-2} for the OER. The inset shows the chronoamperometric curve of the $FeCo_2O_4$ for the OER at a static potential of 1.4 V for 20 h.

(Fig. 1(d)). Their OER activities were then compared with those of highly active electrocatalysts recently published in the literature (Table S1). Among them, $FeCo_2O_4$ MMOFs showed an excellent catalytic activity with a current density of 10 mA·cm^{-2} at a bias of 1.394 V (vs. RHE) and a small Tafel slope (61 mV·dec^{-1}) in alkaline media. Figure S4 shows gas chromatography (GC) curves of $FeCo_2O_4$ before and after the OER at the given current density of 10 mA·cm^{-2}. The GC results clearly confirm that the produced bubbles are O_2. The (FE) and the average oxygen production were measured from the samples ACo_2O_4 for the OER (Fig. 1(e)). The 98.6 % FE of $FeCo_2O_4$ confirms that the current is mainly related to water oxidation reaction (Fig. 1(e)). After testing with the continuous cyclic voltammetry characterization for 10,000 cycles at a scanning rate of 100 mV·s^{-1}, the $FeCo_2O_4$ still exhibited a polarization curve with a stable overpotential of 140 mV at 10 mA·cm^{-2} (Fig. 1(f)). Fig. 1(f) inset shows that the $FeCo_2O_4$ electrolyzer can retain a current density of 10 mA·cm^{-2} over 20 h of continuous operation without any distinct degradation. After the durability test, the morphology of catalysts was characterized (Fig. S5). The results showed good stability for 20 h. The concentrations of Co and Fe were detected by inductively coupled plasma mass spectrometry (ICP-MS). The levels of Co and Fe in the solution after the durability test were 0.4 and 0.2 µg·L^{-1}, respectively.

Morphology features of the as-obtained $FeCo_2O_4$ were further characterized using SEM. The image of $FeCo_2O_4$ shown in Fig. 2(a) reveals that the sample surface is covered with flower-like particulates (with an average size of 2 µm) formed by dozens of nanoplates with an average thickness of around 60 nm. Energy-dispersive X-ray spectroscopy (EDX) mapping analysis (Fig. 2(b)) reveals that iron, cobalt, and oxygen elements are homogeneously distributed in the $FeCo_2O_4$ sample with the molar ratio of oxygen (46.92 at%), iron (14.49 at%), cobalt (29.31 at%), and carbon (9.27 at%). The Fe/Co ratio is determined to be 1/2 (inset of Fig. 2(a)).

Further analysis of these nanoplate structures using TEM reveals that they are mesoporous structures (Fig. 2(c)) composed of nanoparticles with an average size of about 12 nm (Fig. 2(d)). Fig. 2(d) displays a representative HRTEM image of the $FeCo_2O_4$ nanoparticles. The lattice parameter indicated by the arrows in Fig. 2(d) was measured to be 0.22 nm, corresponding to the (311) crystal plane of $FeCo_2O_4$. The nanoplates were further characterized using the selective area electron diffraction (SAED). The four marked diffraction rings in Fig. 2(e) correspond to the (220), (311), (511), and (440) planes of $FeCo_2O_4$.

The porosity of the $FeCo_2O_4$ nanoplates can be determined by N_2 sorption analysis (Fig. 2(f)–(g)). The sample exhibits a typical IV type isotherm with a type H3 hysteresis loop, which confirms that this material has a mesoporous structure with an average pore diameter of 17.4 nm. The BET surface area was around 42 m^2·g^{-1}.

Surface chemical composition and element oxidation states of the $FeCo_2O_4$ MMOFs were analyzed using XPS. Fig. 3(a) displays the C 1*s* spectrum of $FeCo_2O_4$ MMOFs. The peaks at 288.4 and 286 eV are assigned to the O–C=O and C–O–C from the pure

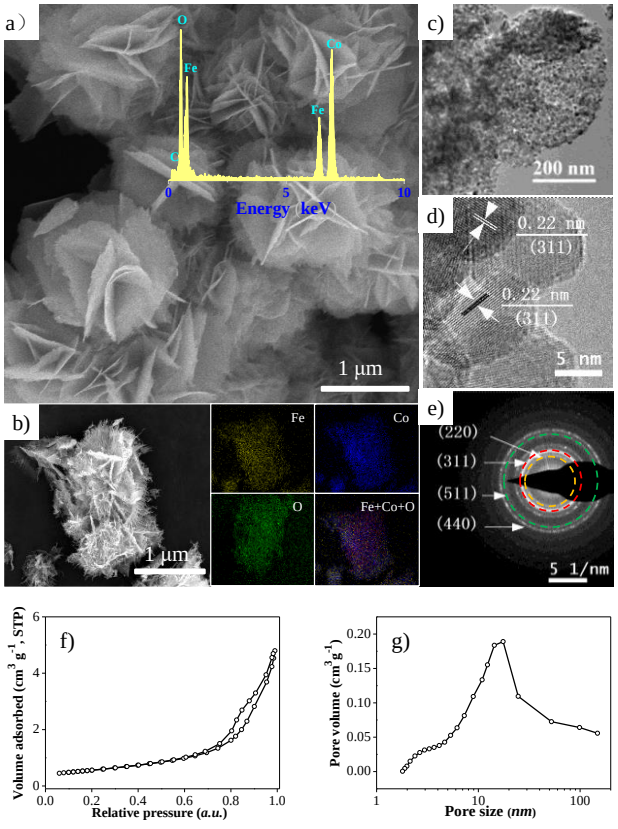

Fig. 2. (a) FESEM images of $FeCo_2O_4$, the inset shows EDX analysis; (b) Element mapping images of $FeCo_2O_4$ for Fe, Co, O, and the RGB images composed of three elemental maps; (c) Transmission electron microscopy (TEM) images; (d) HR-TEM image and the corresponding SAED patterns of $FeCo_2O_4$; N_2 adsorption-desorption isotherms (f) and the pore size distribution (g) of $FeCo_2O_4$, respectively.

PTCDA cyclic anhydride, whereas the peak at 284.4 eV is assigned to the C–C. Figure 3(b) shows the O 1*s* spectrum of $FeCo_2O_4$ MMOFs. The peaks at 533.6, 532, and 530.5 eV are assigned to the O–C=O, C=O, and C–O from the PTCDA cyclic anhydride, whereas the peak at 529.1 eV is assigned to the M–O (where M represents the metal). In the Co 2*p* spectra (Fig. 3(c)), two types of Co species (Co^{2+} and Co^{3+}) are obtained. The binding energies at 782.1 and 797.5 eV are ascribed to Co^{2+}. Another two fitting peaks at 780.1 and 795.4 eV are ascribed to Co^{3+}. These results indicate the co-existence of the Co(II) and Co(III) in $FeCo_2O_4$ (e.g., $Co^{3+}/Co^{2+}{}_{ratio}$ = 2.0, estimated from the ratio between the corresponding peak areas). In the Fe 2*p* spectra (Fig. 3(d)), three types of Fe species (Fe^0, Fe^{2+}, and Fe^{3+}) are detected. The fitted peak at 706.3 eV is ascribed to Fe^0, the fitted peaks at 709.9 and 726.0 eV are ascribed to Fe^{2+}, and the fitted peaks at 712.3 and 728.7 eV are ascribed to Fe^{3+}. These results indicate that the iron in $FeCo_2O_4$ has mixed valences ($Fe^0/Fe^{2+}/Fe^{3+}{}_{ratio}$ = 1/15/10, estimated from the corresponding peaks areas). The valence values are identified to change from single to mixed for Fe and Co ions.

When the Fe cations hop through the tetrahedral-trigonal-octahedral paths, the numbers of Fe cations increase, and thus a Bader charge of +1.92 e changes into charges of +2.82 e and +2.83 e at the trigonal transition state (TS) and the tetrahedral saddle-point state (SS), respectively. This suggests that the valence state of Fe increases when the Fe cation diffuses from the octahedron to the tetrahedron position. The Co cations also diffuse by moving through the octahedral–trigonal–tetrahedral path as described above but with an activation energy of 1.3 eV and formation energy into a tetrahedral intermediate of 1.2 eV. The Bader charge of Co changes from +2.92 e to +1.82 e and +1.83 e at the TS and SS states, respectively. This indicates that the valence state of Co is reduced when the Co cation diffuses from the octahedron to the tetrahedron position. The valence values of Fe and Co, which are obtained from the DFT analysis, are consistent with the XPS results (Fig. 3(c) and 3(d)).

Figure 4(a) illustrates the diffusing paths of metal ions from

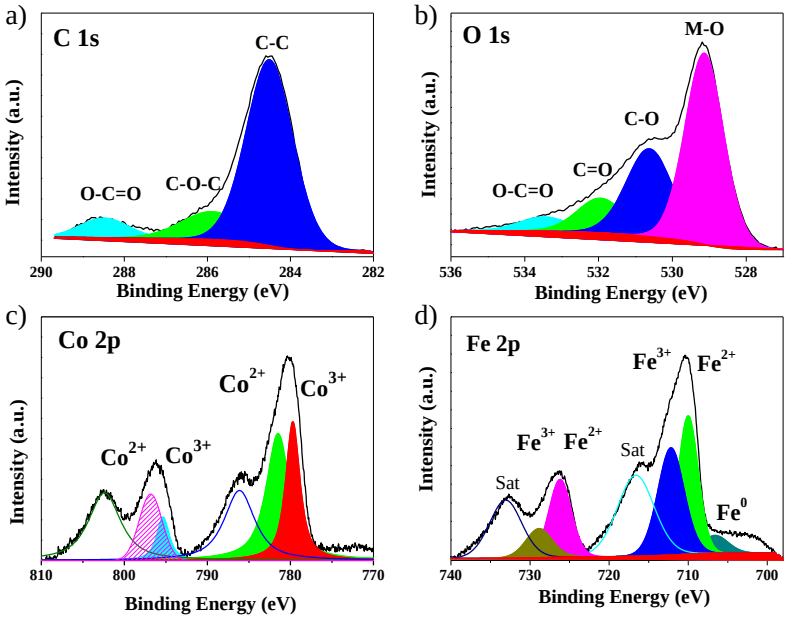

Fig. 3. XPS analysis of $FeCo_2O_4$ MMOFs. (a) C 1*s*; (b) O 1*s*; (c) Co 2*p*; (d) Fe 2*p*.

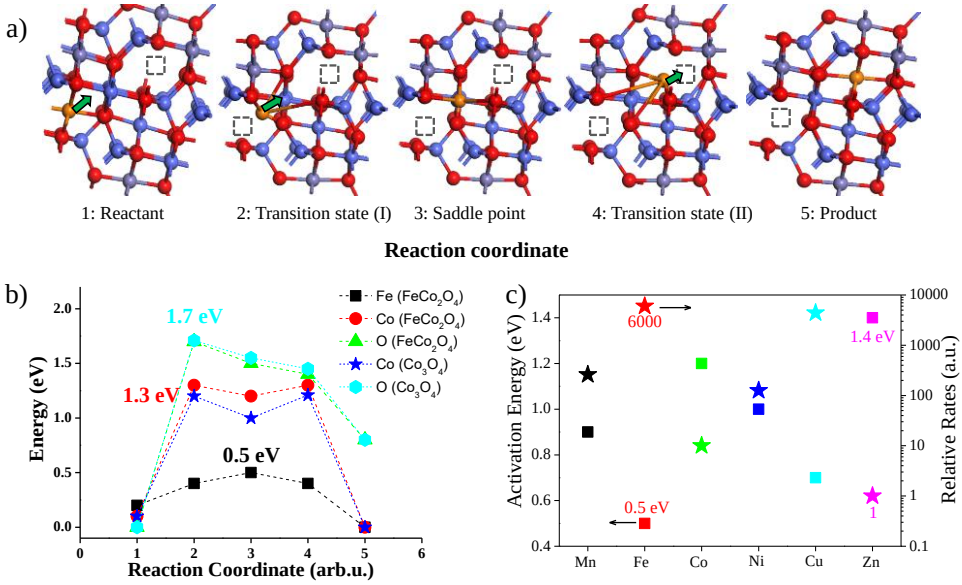

Fig. 4. (a) Geometries of a migrating cation at unique positions along the reaction path. The five representative figures show the initial position of the cation in the octahedral site (1), the cation in the trigonal transition state (I) geometry (2), the cation in the tetrahedral saddle-point geometry (3), the cation in the trigonal transition state (II) geometry (4) and the final position of the cation in the octahedral site (5). The reaction coordinate labels correspond with those of the diffusion potential energy plot. Color scheme: gold sphere for migrating cation, blue for Co, gray for Fe, and red for O. The dotted squares and green arrows indicate cationic vacancies and the direction of the migrating cation along the reaction path, respectively. (b) Hopping activation energies for octahedral-octahedral migration for Fe, Co, and O ions in $FeCo_2O_4$ and Co ion in Co_3O_4; (c) Activation energies and relative rates for cations (A = Mn, Fe, Co, Ni, Cu, and Zn) hopping in ACo_2O_4.

the initial octahedral sites to the neighboring octahedral vacancies via a saddle-point plane. As shown in Fig. 4(b), the obtained hopping activation energies of Fe, Co, and O diffusions are 0.5, 1.3, and 1.7 eV, respectively. The obtained hopping activation energies of cationic (Fe and Co) diffusion for octahedral-octahedral migrations are lower than those of anionic (oxygen) diffusion. This can be attributed to the considerably higher equilibrium concentration of cation vacancies than those of oxygen vacancies in the ACo_2O_4 under the OER conditions. Recent studies proved that the crucial step for the OER was the cation diffusion in the spinel catalysts [12,32,33].

The conductivity of catalysts is linked closely with the hopping activation energies, which govern the hopping rate of ion diffusion [12,34,35]. We used DFT-based atomistic modeling to calculate the hopping activation energies of ion diffusion processes. Fig. 4(c) depicts the obtained hopping energies for A (A = Mn, Fe, Co, Ni, Cu, and Zn) ions in ACo_2O_4 crystals at 25 °C. The hopping activation barrier energies of Fe (0.5 eV) are much smaller than those of Cu (0.7 eV), Mn (0.8 eV), Ni (1.0 eV), Co (0.95 eV), and Zn (1.4 eV) in ACo_2O_4. Based on the ratios of the Arrhenius equations for the various migrations and their associated activation energies [12], the relative rates of cationic hopping through the ACo_2O_4 spinels were calculated, and the results are shown in Fig. 4(c). Clearly, the order sequence of the relative rates is as follows: $FeCo_2O_4$ > $CuCo_2O_4$ > $MnCo_2O_4$ > Co_3O_4 >$NiCo_2O_4$ > $ZnCo_2O_4$.

Electrical impedance spectroscopy (EIS) characterization (in Fig. S6) was further performed to study the effect of substitution of A on the electrical resistance of the ACo_2O_4 electrodes. The charge transfer between the catalyst and electrolyte was an important indicator for evaluating the catalytic properties. EIS was utilized to analyze the behavior of charge transfer at the interface or the surface. Huge difference in the charge-transfer resistance (R_{in}) was observed for these ACo_2O_4 electrodes, ranging from the lowest value of $FeCo_2O_4$ (12.9 $\Omega \cdot cm^{-2}$) to the highest value of $ZnCo_2O_4$ (992 $\Omega \cdot cm^{-2}$). Therefore, the high electrical conductivity and faster charge transport of the $FeCo_2O_4$ as an electrode can guarantee its excellent OER performance [36].

When the A-site element is substituted with the transition metal elements Mn, Fe, Co, Ni, Cu, to Zn in a sequence, the electron numbers of the corresponding outer d-orbitals change from 5 to 10. The ions of metal elements existed in the form of Zn^{2+}, Mn^{2+}, and Cu^{+}, whereas the elements Ni, Co, and Fe exhibited various oxidation states based on the XPS results (Fig. 5). According to the crystal field (CF) theory [37], the preference of an element to be in octahedral or tetrahedral geometry is mainly determined by the octahedral site preference energy (OSPE), which is defined as the difference between the crystal field splitting energy (CFSE) of the octahedral complex and a tetrahedral complex. To compare the preferences of forming an octahedral field or tetrahedral field, the OSPE can be written as:

$$OSPE = CFSE_{(oct)} - CFSE_{(tet)} \quad (4)$$

From Equation 4, the OSPE value as a function of the number of d-electrons can be calculated. The order of OSPE values for all the cations can be ranked as follows: Ni^{2+} > Fe^{2+} > Co^{3+} > Co^{2+} > Fe^{3+} > Mn^{2+}> Cu^{2+} > Zn^{2+}.

The elements Mn^{2+}, Cu^{+}, and Zn^{2+} preferably occupy a tetrahedral position, but the elements of Ni^{2+} and Fe^{2+} prefer an octahedral position. The OSPE values of Ni^{2+} and Fe^{2+} are larger

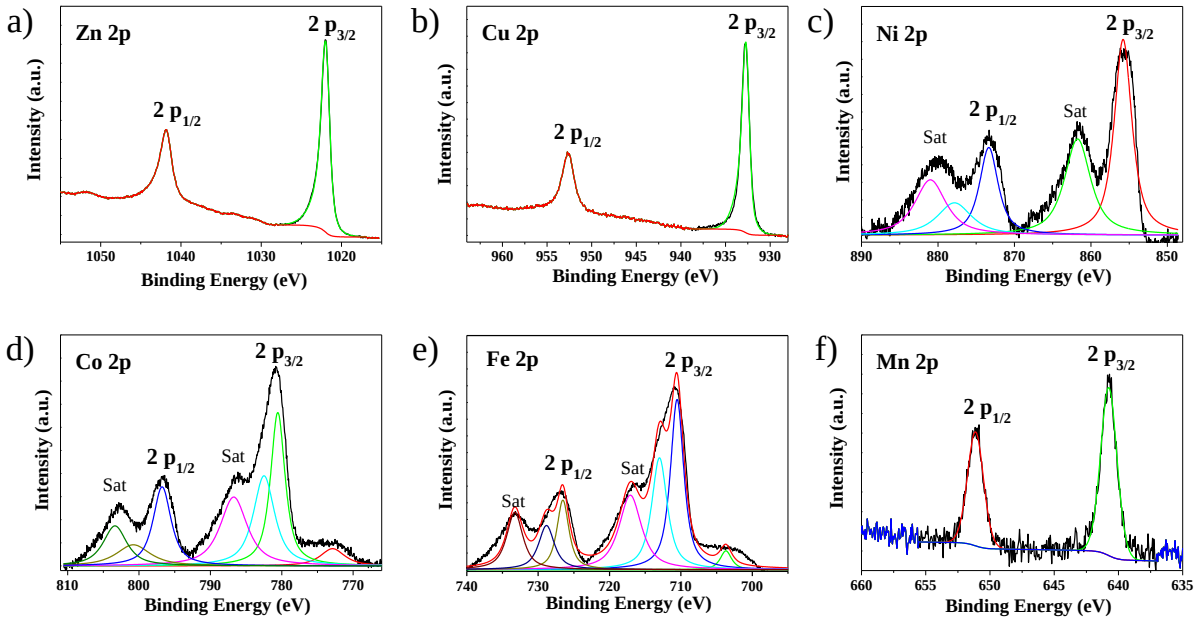

Fig. 5. XPS analysis for Zn 2*p* in $ZnCo_2O_4$ (a), Cu 2*p* in $CuCo_2O_4$ (b), Ni 2*p* in $NiCo_2O_4$ (c), Co 2*p* in Co_3O_4 (d), Fe 2*p* in $FeCo_2O_4$ (e), and Mn 2*p* in $MnCo_2O_4$ (f).

than that of Co^{3+}, so these cations in the tetrahedron can be exchanged with the octahedral Co^{3+}. The cations A' valence state and distribution can be obtained from the state density of ACo_2O_4 crystal (Fig. S7) and X-ray absorption spectroscopy (XAS) [12,17]. For the Fe^{2+} ions, the results showed that exchange between Fe(Td) ↔ Co(Oh) easily occur. Thus, Fe can occupy both octahedron and tetrahedron positions. This might be the reason why the $FeCo_2O_4$ can easily form composite hybrid spinel structures. Our findings are supported by previous reports that the cations A' valence values depend on the occupied positions [12,14,17]. As stated above, the dominant factor for the OER performance of electrode materials is the spinel crystal field. According to the crystal field theory, the spinel crystal field was identified as the essential parameter to control cation A valence values and occupied positions.

4. Conclusions

In summary, ACo_2O_4 phases (A = Mn, Fe, Co, Ni, Cu, or Zn) were successfully synthesized in this work. Among these, the $FeCo_2O_4$ spinel oxide showed excellent OER catalytic activities with a current density of 10 $mA{\cdot}cm^{-2}$ at an overpotential of 164 mV in alkaline media. Based on our experimental results and theoretical analysis, the spinel crystal field is the dominant factor for the OER performance of electrode materials. The spinel crystal field was further identified as the essential parameter for controlling the hopping activation energies, occupied positions, and valence states of cation A.

Acknowledgments

The authors would like to thank Yan Shen, the Analytical and Testing Center of HUST, and the Center of Micro-Fabrication and Characterization of WNLO for the measurements.

References

[1] C. C. L. McCrory, S. Jung, I. M. Ferrer, S. M. Chatman, J. C. Peters, T. F. Jaramillo, *J. Am. Chem. Soc.*, **2015**, 137, 4347–4357.
[2] G. Chen, J. Du, X. Wang, X. Shi, Z. Wang, H.-P. Liang, *Chin. J. Catal.*, **2019**, 40, 1540–1547.
[3] X. Sun, *Chin. J. Catal.*, **2019**, 40, 1405–1407.
[4] J. Li, Q. Zhuang, P. Xu, D. Zhang, L. Wei, D. Yuan, *Chin. J. Catal.*, **2018**, 39, 1403–1410.
[5] M. Mahdavi, M. B. Ahmad, M. J. Haron, F. Namvar, B. Nadi, M. Z. A. Rahman, J. Amin, *Molecules*, **2013**, 18, 7533–7548.
[6] M. Liu, A. Jain, Z. Rong, X. Qu, P. Canepa, R. Malik, G. Ceder, K. A. Persson, *Energy Environ. Sci.*, **2016**, 9, 3201–3209.
[7] Z. Wang, P. K. Nayak, J. A. Caraveo-Frescas, H. N. Alshareef, *Adv. Mater.*, **2016**, 28, 3831–3892.
[8] T. Tatarchuk, M. Bououdina, J. Judith Vijaya, L. John Kennedy, Springer International Publishing, Cham, **2017**, 305-325.
[9] R. J. Hill, J. R. Craig, G. V. Gibbs, *Phys. Chem. Miner.*, **1979**, 4, 317–339.
[10] Y.-T. Lu, Y.-J. Chien, C.-F. Liu, T.-H. You, C.-C. Hu, *J. Mater. Chem. A*, **2017**, 5, 21016–21026.
[11] C. C. L. McCrory, S. H. Jung, J. C. Peters, T. F. Jaramillo, *J. Am. Chem. Soc.*, **2013**, 135, 16977–16987.
[12] C. L. Muhich, V. J. Aston, R. M. Trottier, A. W. Weimer, C. B. Musgrave, *Chem. Mater.*, **2016**, 28, 214–226.
[13] F. Cheng, J. Shen, B. Peng, Y. Pan, Z. Tao, J. Chen, *Nature Chemistry*, **2010**, 3, 79.
[14] T. Wang, Y. Sun, Y. Zhou, S. Sun, X. Hu, Y. Dai, S. Xi, Y. Du, Y. Yang, Z. J. Xu, *ACS Catal.*, **2018**, 8, 8568–8577.
[15] Yiliguma, Z. Wang, W. Xu, Y. Wang, X. Cui, A. M. Al–Enizi, Y. Tang, G. Zheng, *J. Mater. Chem. A*, **2017**, 5, 7416–7422.
[16] T. H. Lim, S. B. Park, J. M. Kim, D. H. Kim, *J. Mol. Catal. A*, **2017**, 426,

Graphical Abstract

Chin. J. Catal., 2020, 41: 0–0 doi: 10.1016/S1872-2067(20)63638-5

Highly efficient mixed-metal spinel cobaltite electrocatalysts for the oxygen evolution reaction

Leiming Tao, Penghu Guo, Weiling Zhu, Tianle Li, Xiantai Zhou, Yongqing Fu, Changlin Yu *, Hongbing Ji *
Guangdong University of Petrochemical Technology, China;
Huazhong University of Science and Technology, China;
Northumbria University, UK; Sun Yat-sen University, China

Cation substitution of spinel cobaltites is a promising strategy for optimizing the electrochemical performance for water splitting. The $FeCo_2O_4$ has an overpotential of 164 mV at a current density of 10 mA·cm^{-2} in alkaline media. The underlying mechanisms have been clarified by cation substitution with different numbers of d-electrons between 5 and 10. The crystal field of spinel ACo_2O_4 is identified as the key factor in dictating the OER performance of these spinel cobaltites.

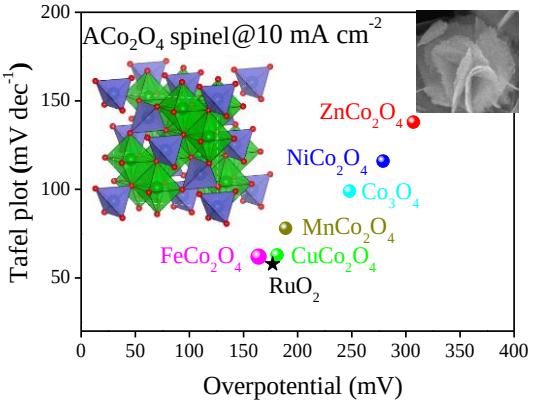

68–74.
[17] C. Wei, Z. X. Feng, G. G. Scherer, J. Barber, Y. Shao-Horn, Z. C. J. Xu, *Adv. Mater.*, **2017**, 29, 1606800.
[18] X. Liu, Z. Chang, L. Luo, T. Xu, X. Lei, J. Liu, X. Sun, *Chem. Mater.*, **2014**, 26, 1889–1895.
[19] M. Prabu, K. Ketpang, S. Shanmugam, *Nanoscale*, **2014**, 6, 3173–3181.
[20] G. S. Hutchings, Y. Zhang, J. Li, B. T. Yonemoto, X. Zhou, K. Zhu, F. Jiao, *J. Am. Chem. Soc.*, **2015**, 137, 4223–4229.
[21] J. Zhao, F. Wang, P. Sun, M. Li, J. Chen, Q. Yang, C. Li, *J. Mater. Chem.*, **2012**, 22, 13328–13333.
[22] T. Shinagawa, A. T. Garcia-Esparza, K. Takanabe, *Sci. Rep.*, **2015**, 5, 13801.
[23] S. Zhao, Y. Wang, J. Dong, C.-T. He, H. Yin, P. An, K. Zhao, X. Zhang, C. Gao, L. Zhang, J. Lv, J. Wang, J. Zhang, A. M. Khattak, N. A. Khan, Z. Wei, J. Zhang, S. Liu, H. Zhao, Z. Tang, *Nature Energy*, **2016**, 1, 16184.
[24] A. J. Bard, L. R. Faulkner, *J. Chem. Educ.*, **2001**, 60, 80–89.
[25] J. P. Singh, R. N. Singh, *J. New Mater. Electrochem. Syst.*, **2000**, 3, 137–146.
[26] S. Gao, Y. Lin, X. C. Jiao, Y. F. Sun, Q. Q. Luo, W. H. Zhang, D. Q. Li, J. L. Yang, Y. Xie, *Nature*, **2016**, 529, 68–+.
[27] B. Iandolo, B. Wickman, B. Seger, I. Chorkendorff, I. Zorić, A. Hellman, *Phys. Chem. Chem. Phys.*, **2014**, 16, 1271–1275.
[28] G. Kresse, J. Furthmüller, *Phys. Rev. B*, **1996**, 54, 11169–11186.
[29] G. Kresse, D. Joubert, *Phys. Rev. B*, **1999**, 59, 1758–1775.
[30] J. P. Perdew, K. Burke, M. Ernzerhof, *Phys. Rev. Lett.*, **1996**, 77, 3865–3868.
[31] S. L. Dudarev, G. A. Botton, S. Y. Savrasov, C. J. Humphreys, A. P. Sutton, *Phys. Rev. B*, **1998**, 57, 1505–1509.
[32] F. Li, Z. Sun, S. Luo, L.-S. Fan, *Energy Environ. Sci.*, **2011**, 4, 876–880.
[33] L. Yuan, Y. Wang, R. Cai, Q. Jiang, J. Wang, B. Li, A. Sharma, G. Zhou, *Mater. Sci. Eng.*, **2012**, 177, 327–336.
[34] R. Pornprasertsuk, P. Ramanarayanan, C. B. Musgrave, F. B. Prinz, *J. Appl. Phys.*, **2005**, 98, 103513.
[35] M. Asnavandi, Y. Yin, Y. Li, C. Sun, C. Zhao, *ACS Energy Lett.*, **2018**, 3, 1515–1520.
[36] K. Liang, L. Guo, K. Marcus, S. Zhang, Z. Yang, D. E. Perea, L. Zhou, Y. Du, Y. Yang, *ACS Catal.*, **2017**, 7, 8406–8412.
[37] R. G. Burns, *Mineralogical Applications of Crystal Field Theory*, Cambridge University Press, **1993**.

Supporting Information for

Highly efficient mixed-metal spinel cobaltite electrocatalysts for the oxygen evolution reaction

Leiming Tao [a,b], Penghu Guo [a], Weiling Zhu [a], Tianle Li [a], Xiantai Zhou [d], Yongqing Fu [c], Changlin Yu [a, #], Hongbing Ji [a,d, *]

[a] *School of Science, Guangdong University of Petrochemical Technology, Maoming 525000, Guangdong, China*
[b] *Wuhan National Laboratory for Optoelectronics, Huazhong University of Science and Technology, Wuhan 430074, Hubei, China*
[c] *Faculty of Engineering and Environment, Northumbria University, Newcastle upon Tyne, NE1 8ST, UK*

[d] Fine Chemical Industry Research Institute, School of Chemistry, Sun Yat-sen University, Guangzhou 510275, Guangdong, China

* Corresponding author. Tel/Fax: +86-0668-2923081; E-mail: jihb@mail.sysu.edu.cn
# Corresponding author. E-mail: yuchanglinjx@163.com

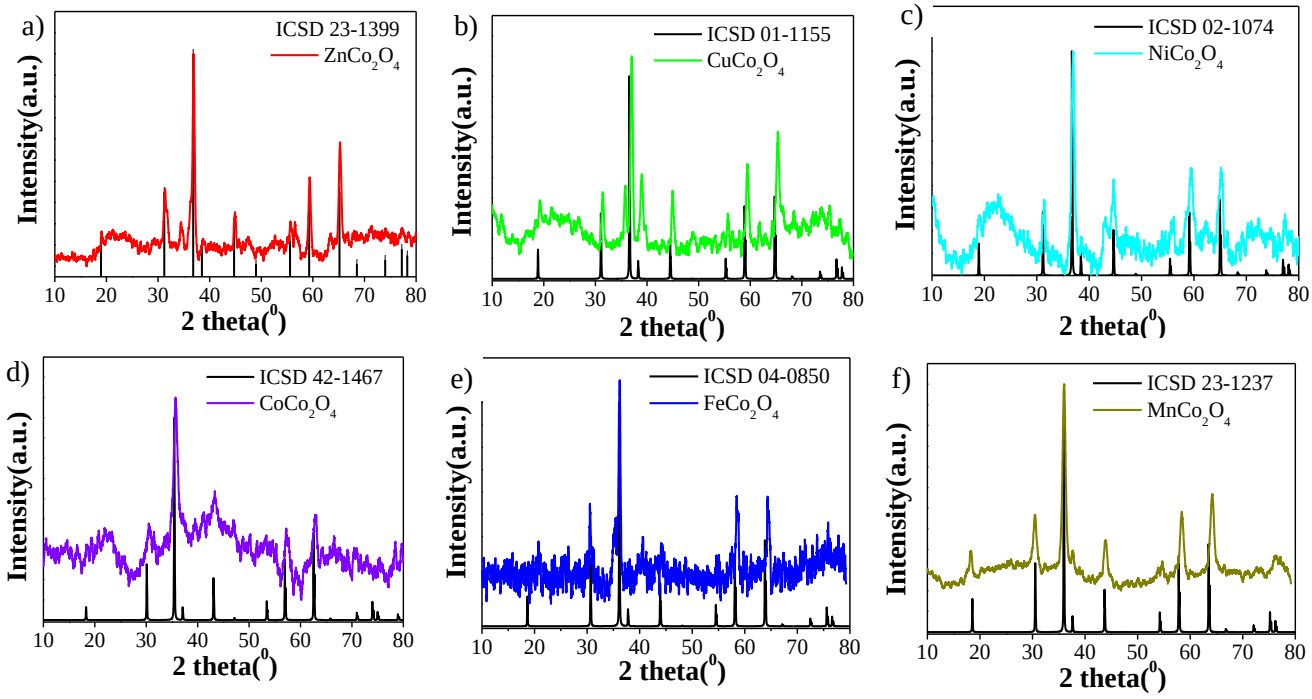

Fig. S1. XRD patterns of different metal cobalt oxides (a) $ZnCo_2O_4$, (b) $CuCo_2O_4$, (c) $NiCo_2O_4$, (d) Co_3O_4, (e) $FeCo_2O_4$, and (f) $MnCo_2O_4$.

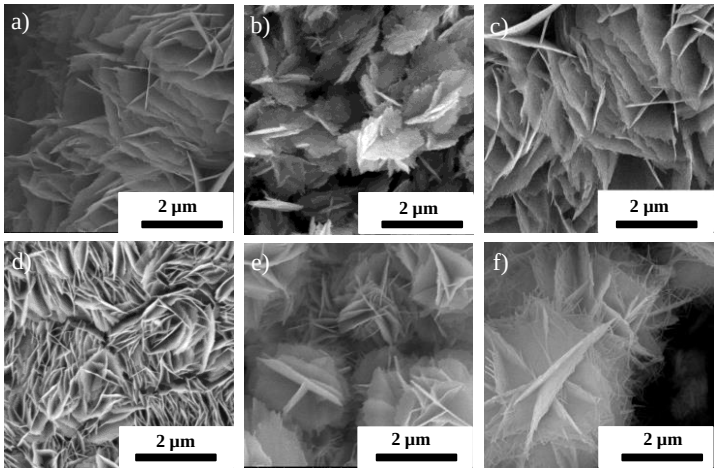

Fig. S2. Field-emission scanning electron microscope (FESEM) images of (a) $ZnCo_2O_4$, (b) $CuCo_2O_4$, (c) $NiCo_2O_4$, (d) Co_3O_4, (e) $FeCo_2O_4$, and (f) $MnCo_2O_4$.

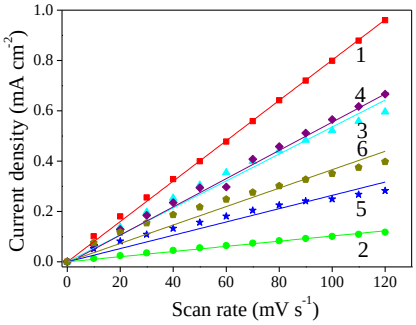

Fig. S3. The capacitive currents with various scan rates (10, 20, 30, 40, 50, 60, 70, 80, 90, 100, 110, and 120 mV s^{-1}) collected for estimating the double-layer capacitance (C_{dl}) in the potential region 0 – 0.05 V vs Hg/HgO in 1 M KOH; $ZnCo_2O_4$ (curve 1), $CuCo_2O_4$ (curve 2), $NiCo_2O_4$ (curve 3), Co_3O_4 (curve 4), $FeCo_2O_4$ (curve 5) and $MnCo_2O_4$ (curve 6).

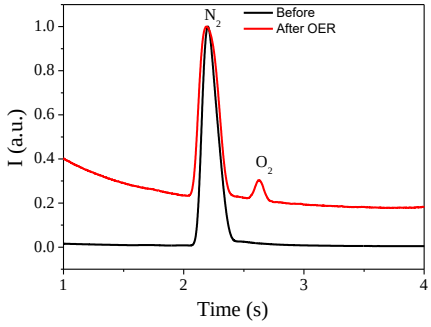

Fig. S4. Gas chromatography curves of $FeCo_2O_4$ before and after OER.

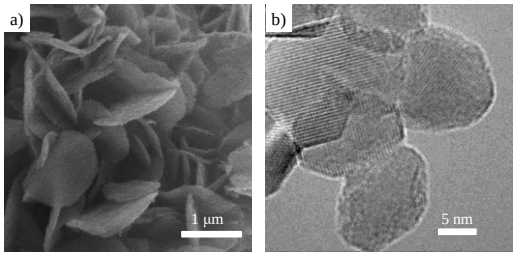

Fig. S5. a) FESEM images and b) TEM images for $FeCo_2O_4$ after 20h with the current density increased from 10 mA·cm^{-2}.

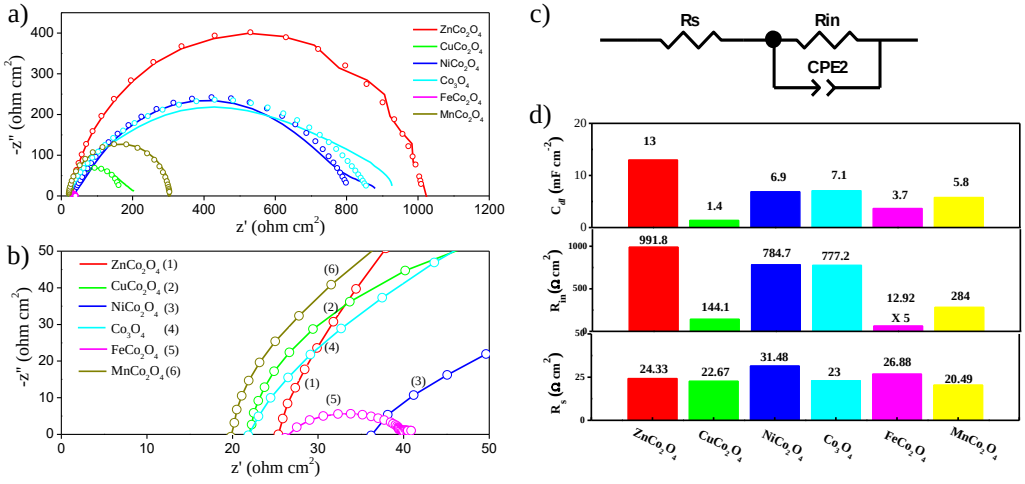

Fig. S6. Electrochemical impedance spectroscopy of a) and b) the corresponding magnified view for $ZnCo_2O_4$ (curve 1), $CuCo_2O_4$ (curve 2), $NiCo_2O_4$ (curve 3), Co_3O_4 (curve 4), $FeCo_2O_4$ (curve 5), and $MnCo_2O_4$ (curve 6) electrodes recorded at 0.5 V vs Hg/HgO; c) the equivalent circuit of the cells; d) the date of the double-layer capacitance (C_{dl}), series resistor (R_s) and parallel resistor (R_{in}) fitted with the simplified equivalent circuit, respectively.

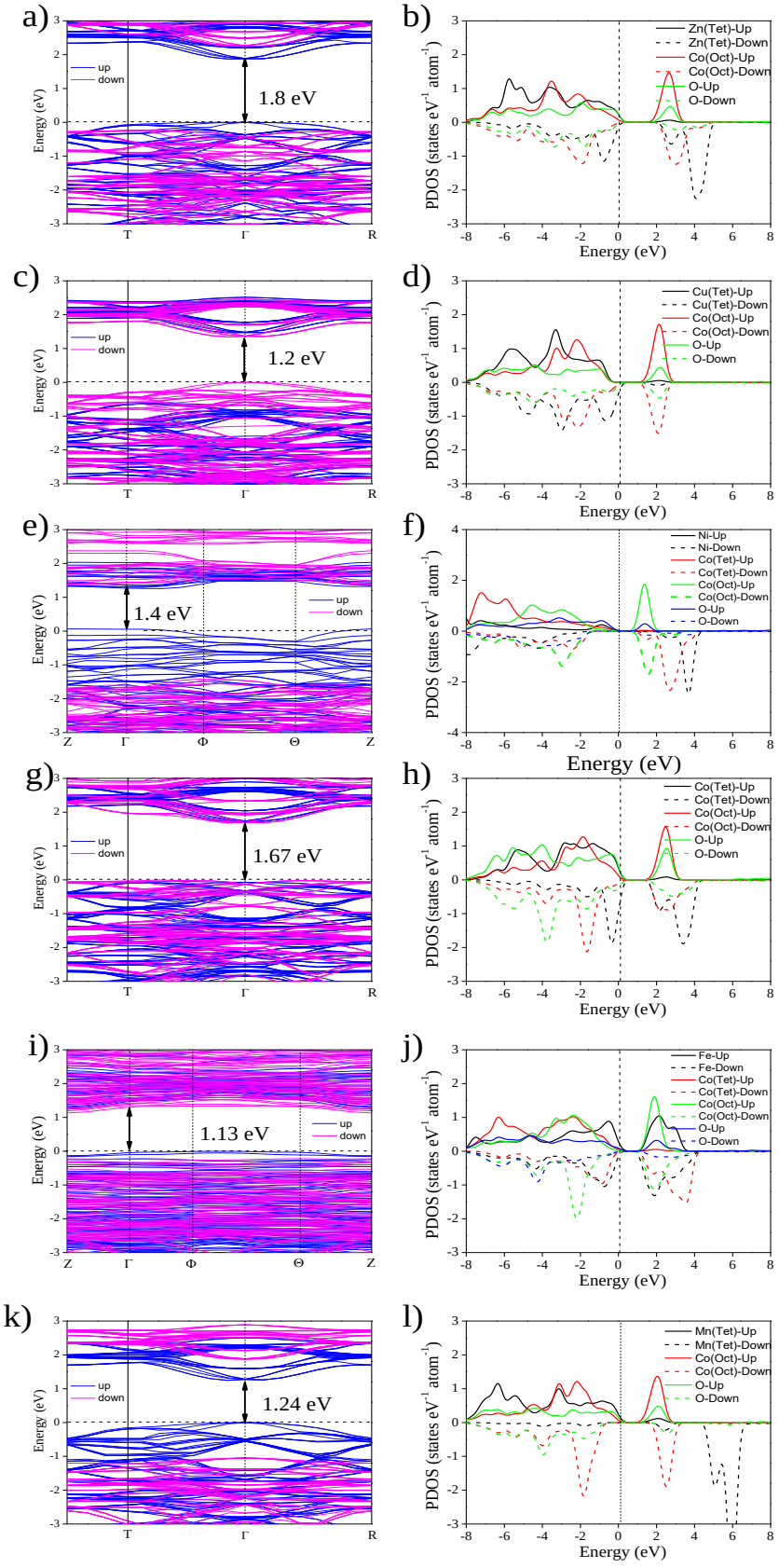

Fig. S7. Electronic band structures for the spin-up states (blue) and spin-down states (pink), and projected density of states (PDOS) for tetrahedral (Tet) sites and octahedral (Oct) sites of $ZnCo_2O_4$ (a and b), $CuCo_2O_4$ (c and d), $NiCo_2O_4$ (e and f), Co_3O_4 (g and h), $FeCo_2O_4$ (i and j), and $MnCo_2O_4$ (k and l) calculated using density functional theory (DFT)+U, respectively. The spin-up PDOS are shown on a positive scale (solid line), while spin-down PDOS are shown on a negative scale (dashed line). The Fermi level is aligned to 0 eV.

Table S1
Comparison of OER activity for $FeCo_2O_4$ with other recently published highly active electrocatalysts in alkaline electrolyte (1 M KOH). Unless stated otherwise, the tests were made in 1.0 M KOH solution.

Catalyst	OER		Reference
	η_{OER} (mV) 10 mA·cm^{-2}	Tafel (mV·decade^{-1})	
$FeCo_2O_4$	164	61	This work
$NiCo_2O_4$-nanowire	240	70	*J. Phys. Chem. C*, 2017, 121, 25888.[1]
$NiCo_2O_4$-nanosheet	260	53	
$NiCo_2O_4$@NiO@Ni Core/Shell Nanocone Array	240	58	*Part. Part. Sys. Char.*2017, 34, 1700228.[2]
$NiCo_2O_4$/NF	240	51.5	*Adv. Func. Mater.*, 2016, 26, 3515.[3]
NiFe-LDH/$NiCo_2O_4$ /NF	230	53	*ACS Appl. Mater. Int.* 2017, 9, 1488.[4]
$NiCo_2O_4$ nanosheet array	270	51.9	*J. Catal.* 2018, 357, 238.[5]
IrO_X/C	210	139	Angew. Chem. Int. Edit. 2018, 57,15445. [6]
S:Co_2P@NF	288	71	Chem. Mater. 2018, 30, 8861. [7]
CdS/Ni_3S_2/PNF	151	174	ACS Appl. Mat. Interfaces 2017,9, 29660. [8]
NiS/Ni	83	89	Chem. Commun.2016, 52, 1486. [9]
Co_4NiP	239	45	Adv. Funct. Mater.2016, 26, 7644. [10]
$NiCo_2S_4$	210	40.1	Adv. Funct. Mater. 2016, 26, 4661. [11]
NiSe/NF	270	64	Angew. Chem. Int. Edit. 2015, 54, 9351. [12]
Ni/NiP	260	73.2	Adv. Funct. Mater. 2016, 26, 3314. [13]

References

[1] L. M. Tao, Y. B. Li, M. Li, G. Y. Gao, X. Xiao, M. K. Wang, X. X. Jiang, X. W. Lv, Q. W. Li, S. S. Zhang, Z. X. Zhao, C. Zhao, Y. Shen, *J. Phys. Chem. C*, **2017**, 121, 25888–25897.

[2] L. Y. Wang, C. D. Gu, X. Ge, J. L. Zhang, H. Y. Zhu, J. P. Tu, *Part Part Syst. Char.*, **2017**, 34, 1700228.

[3] C. L. Xiao, Y. B. Li, X. Y. Lu, C. Zhao, *Adv. Funct. Mater.*, **2016**, 26, 3515–3523.

[4] Z. Wang, S. Zeng, W. Liu, X. Wang, Q. Li, Z. Zhao, F. Geng, *ACS Appl. Mat. Interfaces*, **2017**, 9, 1488–1495.

[5] L. Fang, Z. Jiang, H. Xu, L. Liu, Y. guan, X. Gu, Y. Wang, *J. Catal.*, **2018**, 357, 238–246.

[6] R. Wu, B. Xiao, Q. Gao, Y. R. Zheng, X. S. Zheng, J. F. Zhu, M. R. Gao, S. H. Yu, *Angew. Chem. Int. Ed.*, **2018**, 57, 15445–15449.

[7] M. A. R. Anjum, M. D. Bhatt, M. H. Lee, J. S. Lee, *Chem. Mater.*, **2018**, 30, 8861–8870.

[8] S. Q. Qu, J. Huang, J. S. Yu, G. L. Chen, W. Hu, M. M. Yin, R. Zhang, S. J. Chu, C. R. Li, *ACS Appl. Mat. Interfaces*, **2017**, 9, 29660–29668.

[9] W. X. Zhu, X. Y. Yue, W. T. Zhang, S. X. Yu, Y. H. Zhang, J. Wang, J. L. Wang, *Chem. Commun.*, **2016**, 52, 1486–1489.

[10] J. Yu, Q. Li, Y. Li, C.-Y. Xu, L. Zhen, V. P. Dravid, J. Wu, *Adv. Funct. Mater.*, **2016**, 26, 7644–7651.

[11] A. Sivanantham, P. Ganesan, S. Shanmugam, *Adv. Funct. Mater.*, **2016**, 26, 4661–4672.

[12] C. Tang, N. Y. Cheng, Z. H. Pu, W. Xing, X. P. Sun, *Angew. Chem. Int. Ed.*, **2015**, 54, 9351–9355.

[13] G.-F. Chen, T. Y. Ma, Z.-Q. Liu, N. Li, Y.-Z. Su, K. Davey, S.-Z. Qiao, *Adv. Funct. Mater.*, **2016**, 26, 3314–3323.